Polar Science 21 (2019) 212–223

Contents lists available at ScienceDirect

Polar Science

journal homepage: www.elsevier.com/locate/polar

Year-round observations of sea-ice drift and near-inertial internal waves in the Northwind Abyssal Plain, Arctic Ocean

Yusuke Kawaguchi[a,*], Motoyo Itoh[b], Yasushi Fukamachi[c,d,e], Erika Moriya[f], Jonaotaro Onodera[b], Takashi Kikuchi[b], Naomi Harada[b]

[a] Atmosphere and Ocean Research Institute, The University of Tokyo, Kashiwa, Japan
[b] Institute of Arctic Climate and Environmental Research, Japan Agency for Marine-Earth Science and Technology, Yokosuka, Japan
[c] Arctic Research Center, Hokkaido University, Sapporo, Japan
[d] Global Station for Arctic Research, Global Institution for Collaborative Research and Education, Hokkaido University, Sapporo, Japan
[e] Institute of Low Temperature Science, Hokkaido University, Sapporo, Japan
[f] Hydro Systems Development, Inc., Tokyo, Japan

ARTICLE INFO

Keywords:
Arctic ocean
Ice drift
Inertial oscillation
Internal gravity waves
Ice profiling sonar

ABSTRACT

In this study, intra-annual variation of near-inertial internal wave (NIW) in the Arctic Ocean is examined using year-round mooring in the Northwind Abyssal Plain. Our emphasis is on dynamical responses of NIW to local sea-ice variables such as concentration, draft, and drift. We obtained those using a coupling system of ice profiling sonar (IPS) and an acoustic Doppler current profiler (ADCP) deployed at the top of the mooring. According to the wavelet spectrum, the inertial oscillation of ice drift becomes considerably strong during periods of ice formation and decay. Results show that the NIW amplitude in the upper part of the water column responds more sensitively to the sea-ice inertial oscillation than to the mean component of ice drift heading to the northwest. We also conducted an experiment with a mixed-layer slab model using the IPS-ADCP measured ice speed to examine the NIW generation responding to the ice-to-ocean stress. Experiment results suggest that the mixed-layer inertial oscillation is amplified in the early time of ice formation, through the ice-water resonance process. It is then concluded that the mixed-layer inertial current driven by ice drift is the primary driver of the enhanced NIW generation.

1. Introduction

In polar seas, knowledge of turbulence and internal waves in the water is crucially important to quantify the redistribution of heat and kinetic energy (affecting sea ice variation and climate change). Specifically, turbulent mixing in the upper part of the water column can affect the sea ice by modifying the delivery of heat to the bottom of the sea ice and can alter the sea-ice-ocean heat balance (McPhee, 2008). Recent diminishment of the sea ice cover might affect the local climate in multiple ways (e.g., atmospheric boundary layer dynamics, cloud formation, and the shortwave and longwave radiation coming into the water) through reduced insulation effects of the sea ice (e.g., Inoue and Hori, 2011). Therefore, quantifying ocean mixing in the present period of rapidly varying and diminishing sea ice is a fundamentally important step to elucidating how the Arctic climate system works.

In the Arctic Ocean, underice turbulent mixing has been believed to be much less than that in mid-latitude seas (e.g., D'Asaro and Morison, 1992; Pinkel, 2005, 2008; Martini et al., 2014), with a few exceptions (D'Asaro and Morehead, 1991; Kawaguchi et al., 2016). Generally speaking, the low levels of turbulent kinetic energy in the Arctic can be attributed to reduced sea ice motion because of the internal stress among consolidated ice floes. This may subsequently lead to reduction in the kinetic energy entering the upper part of water column. For the combination of tidal current over the rough topography, D'Asaro and Morehead (1991) reported strong signals of internal waves over the Yermak Plateau. Another exceptional example of the energetic internal wave and turbulence events in the Arctic Ocean is documented by Kawaguchi et al. (2016). Their results demonstrate that an anticyclonic coherent eddy captured storm-generated NIWs, where the relative vorticity is negative.

Wintertime direct measurement of sea ice and underice parameters (e.g. ice thickness) is difficult because of the severe environment for human onsite operations and the fundamental necessity of specific platforms such as ice breakers. These necessities present challenges to

* Corresponding author.
E-mail address: ykawaguchi@aori.u-tokyo.ac.jp (Y. Kawaguchi).

https://doi.org/10.1016/j.polar.2019.01.004
Received 24 May 2018; Received in revised form 18 December 2018; Accepted 30 January 2019
Available online 31 January 2019

clarification of the relation between physical ice parameters (concentration, thickness, movement, etc.) and internal wave activity in the upper part of the water column. Nevertheless, long-term data acquisition in the polar environment can be achieved using modern techniques at onsite moorings (e.g., Belliveau et al., 1990; Birch et al., 2000; Fukamachi et al., 2003, 2009; 2017; Krishfield et al., 2014; Martini et al., 2014) and by the development of autonomous instruments (e.g., Krishfield et al., 2008; Padman and Kottmeier, 2000; Kawaguchi et al., 2012; Vivier et al., 2016; Zippel and Thomson, 2016). Padman and Kottmeier (2000) examined high-frequency sea ice motion in the Weddell Sea by using satellite-tracked drifting buoys, and assessed the effects of tidal current on the ice motion.

It is noteworthy that some recent reports have described studies of seasonal variation of fine-scale or turbulent kinetic energy in the upper part of the water columns in terms of ice fraction (e.g., Rainville and Woodgate, 2009; Zippel and Thomson, 2016). Zippel and Thomson (2016) described a comparison of the areal ice fraction and near-surface turbulent energy dissipation using a SWIFT buoy equipped with high-frequency velocity and acceleration sensors. They reported that 50% ice coverage can suppress the development of surface short wave and near-surface turbulent energy in the surface layer.

In situ data necessary to elucidate the linkage between the upper part of the water column wave kinetic energy and the local ice parameters are lacking. Ice thickness and the ice-covered fraction can strongly influence ice floe mobility. Consequently, enhanced ice drift can lead to increasing momentum input to surface water, which eventually engenders the enhancement of NIW kinetic energy and turbulence activity in underlying layers.

This study included year-round mooring observations undertaken to quantify the ice draft, ice motion, and horizontal current velocity in seasonally ice-covered Arctic water. For observations, a combination of an ice profiling sonar (IPS) and an upward-looking acoustic Doppler current profiler (ADCP) deployed around 110 m was used. We examined the seasonal variation of ice parameters and fine-scale internal waves. Special attention was devoted to the linkage and interaction between ice drift and internal wave energy.

This report of that study includes the following sections: a brief description of the data and methods in Section 2, main results from sea-ice observations in Section 3, and results from ADCP current velocity in Section 4. The kinetic energy balance in the upper part of the water column is explained quantitatively in Section 5. The overall study results are summarized in Section 6.

2. Data and methods

The collection of data on sea ice in the upper part of water column was conducted using a mooring system with multiple sensors deployed (74°31.36′N, 161°55.59′W) in the Northwind Abyssal Plain (Fig. 1), where the water depth is 1681 m. The mooring system was equipped with three conductivity-temperature (CT) sensors (SBE 37-SM; Sea-Bird Electronics, Inc.) at nominal depths of 176, 196, and 1320 m (serial numbers of SN2155, 2156, and 2163, respectively). The measurement of ice variables (concentration, drift, and draft) was conducted with an IPS (IPS5 420 kHz; ASL Environmental Sciences) and an upward-looking ADCP (300 kHz Workhorse; Teledyne RD Instruments). Upward-looking ADCP and IPS transducers were deployed respectively at nominal depths of 110 m and 30 m. The mooring observation data are available during September 8, 2013 and September 17, 2014.

The IPS acoustic signals are used to calculate the keel depth and ice concentration (Birch et al., 2000). The ice draft is evaluated at time intervals of 1 s after post-processing screening for thin ice. The screening procedure for thin-ice detection was performed as reported by Fukamachi et al. (2003, 2009; 2017), which specifically examined the IPS and ADCP combined data for the study of thin ice and dense shelf water formation in shallow polar seas (i.e., waters off Sakhalin Island in the Sea of Okhotsk and near Barrow Canyon in the Chukchi Sea). The sound speed of seawater, which is the most important parameter to achieve optimal accuracy, was derived with temperature and salinity obtained using the CT sensor nearest to the IPS transducer and using surface-reflected acoustic signals during open-water periods.

Upward-looking ADCP is used to measure sea-ice drift and water current. Acoustic signals back-reflected by the underside of sea ice were analyzed using the “bottom-tracking” function (Belliveau et al., 1990). Under the bottom-tracking mode, the transducer pings once per hour in the middle of water-profiling observations. The ice speed accuracy was estimated as $\pm$ 1 cm s^{-1}, but it is reduced during periods of partial sea ice cover (e.g. flaw lead). By taking advantage of differences in surface-reflected acoustic signals, the existence of sea ice over the mooring site was estimated based on the ADCP error velocity (Belliveau et al., 1990). We determine sea ice to be present when the error velocity magnitude was below 2 cm s^{-1}. The area was regarded as water surface otherwise.

The ADCP's horizontal currents were used for analyses of internal gravity waves. We acquired 24-s current ensembles consisting of 12 pings every hour, and then interpolated the series to produce an hourly time record. The vertical bin size was 4 m. Current data were available between the approximate depths of 6 m and 104 m (after removal of side lobe interference and blanking distance). The annual pressure record indicated a few notable eddy events, resulting in a blow-down of the mooring system. A correction for the change of installation depth was undertaken by a linear interpolation onto the fixed vertical frame (6–104 m). With respect to the internal wave analysis, the water current within the upper 20 m was discarded to avoid deep ice keel effects. In addition to the ADCP observations, an electromagnetic current meter (The InterOcean S4) was used to measure the single-point horizontal current. The current meter was located at the nominal depth of 210 m. Sampling was done every 2 h.

We created a time series of hourly sea-ice concentration by accumulating the 1-Hz IPS signals in conjunction with the error velocity from the ADCP's bottom-tracking observation. The ice concentration was computed from the temporal occupation of zero ice draft in the hourly time frame, where the negative draft was forcibly set to zero.

3. Sea-ice properties

3.1. Sea-ice concentration

This section presents a description of sea-ice variables derived using the combination of IPS and upward-looking ADCP. The sea-ice concentration (SIC) was nearly unity for the period between mid-October 2013 and the end of July 2014 (Fig. 2a). In October, it was interpreted that the surface water started to freeze and that it became fully covered by ice in a week. Once the surface water was sea-ice-covered, SIC rarely dropped below 0.9 except for recurrent lead openings. The SIC diminished rapidly during the summer. After it had experienced a couple of marked drops in mid-July, it showed a rapid decrease down to zero through August. It is plausible that the recurrent lead openings in July introduced abundant solar heat into the surface water, which might have contributed to the subsequent ice melt.

3.2. Sea-ice draft

Next, we report the ice draft estimation results. Regarding the ice draft evolution, one can infer that the general trend was fundamentally determined by thermodynamical processes of freezing and ablation. In other words, the lowpass-filtered temporal variation at the mooring site approximately represents thermodynamical growth/decay in the neighboring area.

Contrary to the rapid growth in ice concentration observed in the autumn of 2013, the ice draft increased at a much slower, nearly linear rate through the end of winter (Fig. 2b). It was apparently less than 1 m in October 2013, but it grew to nearly 2 m by May 2014. This freezing period had an average growth rate of 1.9 cm day^{-1}, which is equivalent

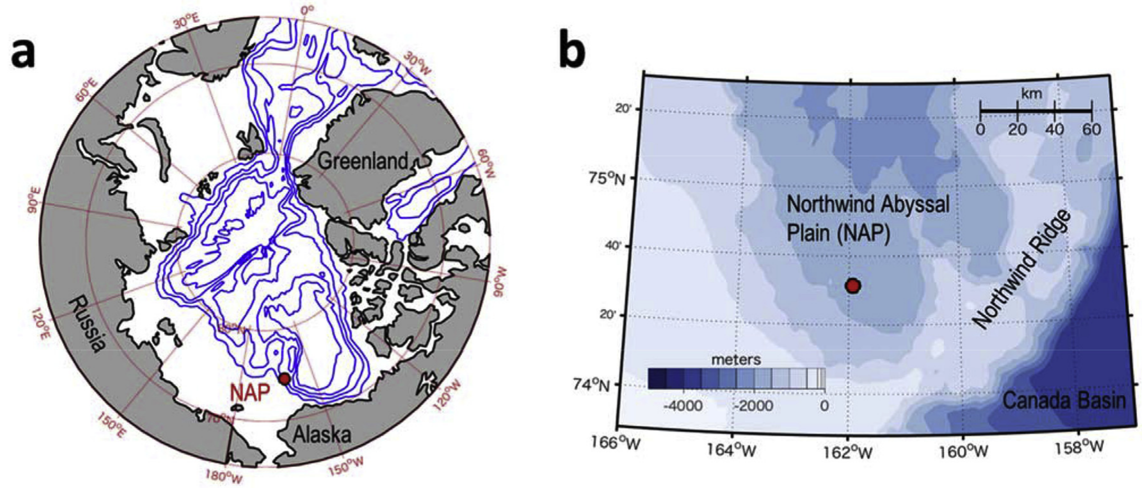

Fig. 1. Maps of (a) the entire Arctic Ocean and (b) study domain in the Northwind Abyssal Plain (NAP). The NAP13t mooring location is denoted as a red circle on both maps. Bathymetric contours are drawn at every 500 m in (a) and according to the color bar in (b).

to 69 W m^{-2} in heat loss for the ice–water interfacial boundary. The latent heat of fusion for sea ice, *LH,* can be calculated as $LH = \rho_{pi} L \frac{\partial H}{\partial t}$, where $\frac{\partial}{\partial t}$ represents the temporal derivative, H stands for the sea ice thickness, the pure ice density ρ_{pi} is 917 kg m^{-3} and the constant for fusion of sea ice L is 333.4 kJ kg^{-1}.

Krishfield et al. (2014) conducted ice draft observations with four IPSs that were remotely deployed in different parts of the Beaufort Gyre (BG). The maximum draft level of 2 m obtained during the 2013–2014 NAP mooring was similar to the results obtained in the southern part of the BG, but 20–50 cm less than results obtained in the northern part of the BG (Krishfield et al., 2014). It is also noteworthy that the ice draft data presented by Krishfield et al. (2014) were acquired in 2004–2010, i.e., different years from those of the present mooring observations.

According to our IPS-ADCP observation, the ice formation phase terminated by early May. The ice draft remained at nearly the same level until the end of June when it started to decrease. The timing of growth/melt transition is similar to those observed in the remaining part of the Arctic Ocean (the North Pole region for Vivier et al., 2016;

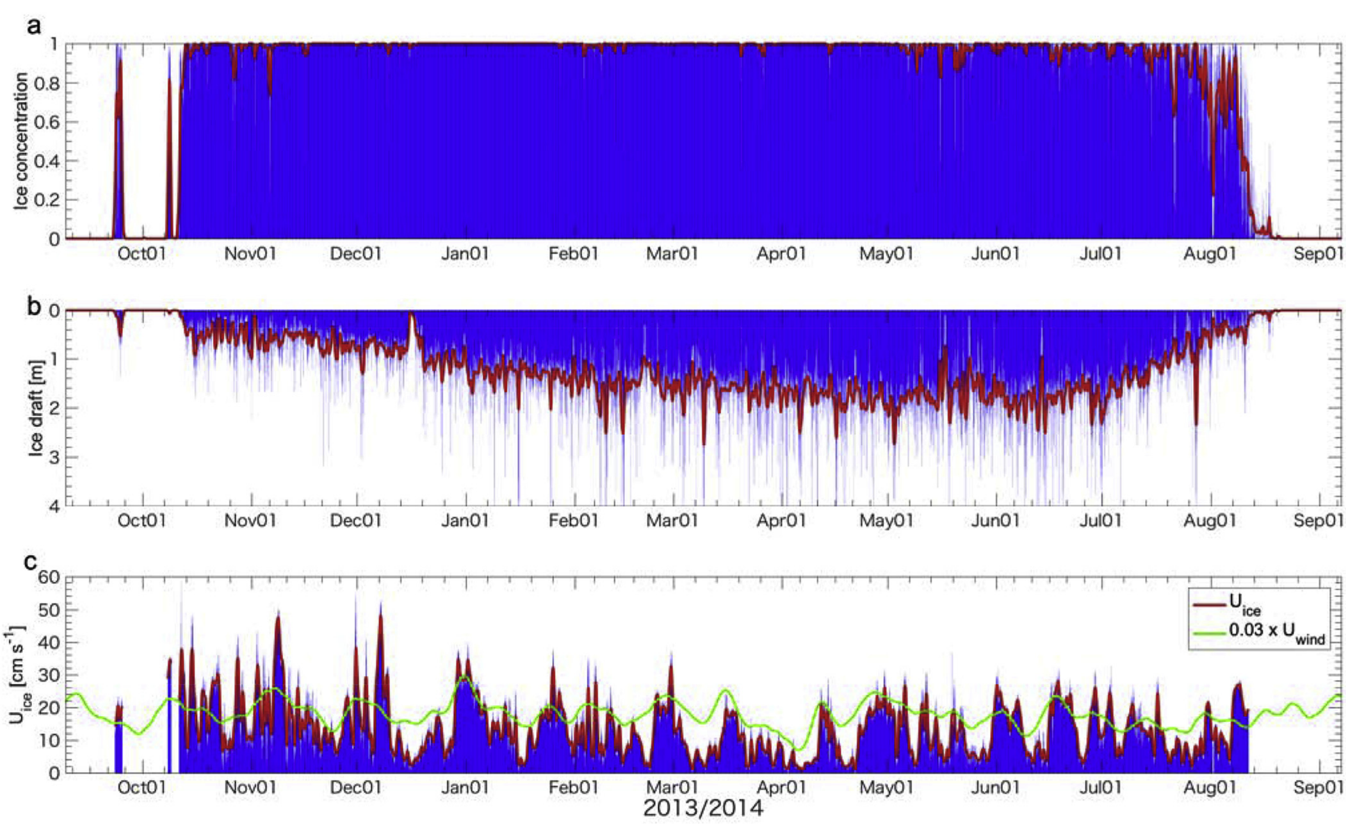

Fig. 2. Time series of IPS-ADCP sea-ice variables: (a) sea-ice concentration (fraction: 0–1); (b) ice draft (m); (c) ice drift magnitude U_{ice} (cm s^{-1}). In each plot, the raw values (in blue bars) are 24-h running averaged, shown by red curves. In (c), 10-m-height wind speed (ERA interim) multiplied by a factor of 0.03 is shown as a green curve for reference (Leppäranta, 2005). On the horizontal axis, only the first day of each month is labelled (e.g. Oct01) as centered on the major ticks. (For interpretation of the references to color in this figure legend, the reader is referred to the Web version of this article.)

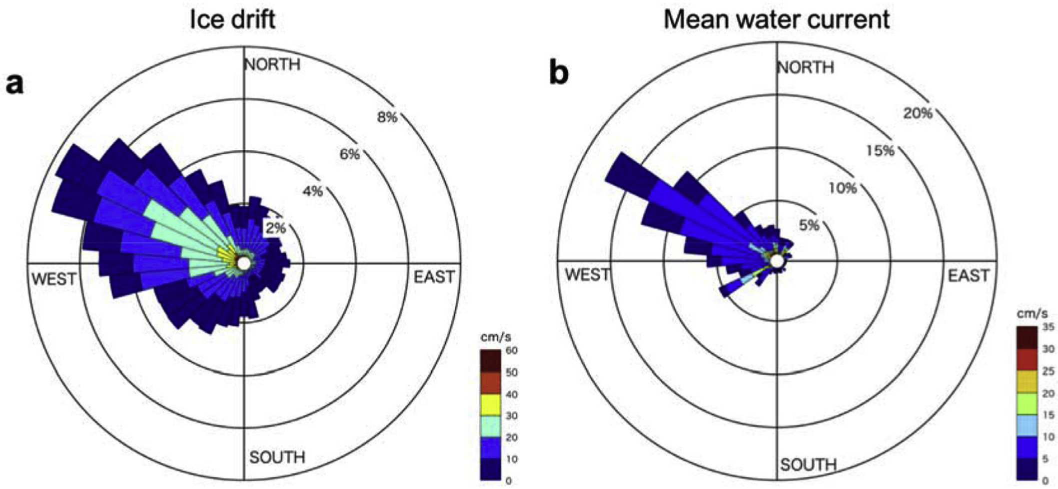

Fig. 3. Rose histograms of (a) ice drift and of (b) water current averaged over depths of 6–104 m.

the BG for Krishfield et al., 2014). After this transition, the moored IPS-ADCP record suggests that the local draft diminished rather rapidly. In fact, the 2-m ice sheet disappeared completely after roughly 50 days by mid-August 2014. The melt rate during this period of diminishment was about 4.1 cm day^{-1}, equivalent to heat gain of 144 W m^{-2} to the ice floe.

3.3. Sea-ice drift

In Fig. 3, the horizontal velocity of ice drift and depth-averaged water current are shown in a rose histogram, where the current is averaged over the upper 104 m (excluding the top 6 m affected by the side lobe effect). According to this plot, the movements in both media were heading in the same direction, to the northwest, i.e. largely following the bathymetric contours. The horizontal speeds were 17 ± 5 cm s^{-1} and 7 ± 2 cm s^{-1}, respectively, for ice drift and the depth-averaged water current. Typically, the ice drift was faster than the average water current, implying that the ice motion dragged the water surface and added momentum to the underlying water column. Magnitude of wind-driven ice drift can be often within a range of a few percentage of surface wind speed, which follows the so-called Zubov's rule for free sea-ice drift (see Chap. 6 in Leppäranta, 2005). According to the time series presented in Fig. 2c, during the early time of ice growth (October – early December), the ice drift magnitude is apparently similar to the level being 3% of the 10-m height wind speed, where the wind data are retrieved from the ERA interim at the nearest grid point. The ice speed is generally below the 3% of surface wind throughout the remainder of the observation period.

To ascertain the sea ice motion periodicity, the Morlet wavelet spectrum of measured sea ice velocity was calculated (Fig. 4). According to the wavelet analysis, the ice motion showed characteristic semidiurnal oscillation (i.e., twice a day) in clockwise (CW) rotation with time. This is regarded as mainly attributable to the inertial movement of sea-ice drift: at the latitude of the mooring site (74.5°N), the Coriolis force gives a periodic oscillation of 12.42 h. The inertial ice motion is the most energetic in the autumn (October through early December; 3.4 cm s^{-1} in amplitude) and the melting season (May–July in the following year; 2.1 cm s^{-1}), although it is the least energetic in the middle of winter (January–April; 1.1 cm s^{-1}). The inertial oscillations in autumn leads the sea ice drift elevation relative to the reference (Fig. 2c). It is added that in February, there is a slight elevation (not statistically significant) near the inertial frequency in CW field. During this time, sea ice concentration shows recurrent diminishing events to reach 0.90–0.95 (Fig. 2a). At those moments, areas of expanded open water and/or newly-forming ice could make ice floes easier to respond to wind. In addition, spectral maxima at frequencies lower than 0.5 CPD exist nearly year-round, where they occur irrespective of the rotational direction. We consider that the slowly fluctuating sea-ice motion reflects the variation in the mean ice flow, i.e. heading to the northwest, as depicted in Fig. 3a.

According to earlier observations taken near the North Pole area (Kawaguchi et al., 2012), sea-ice drift in the inertial oscillation remained negligible until early July. Subsequently, the inertial motion of sea ice built up drastically to reach its maximum in mid-summer: August through mid-September. The present mooring record in NAP indicates an extended period of free ice drift (i.e., in the early summer and late autumn), relative to observations near the North Pole.

4. Near-inertial internal waves in the upper part of the water column

The characteristics of internal waves that propagate in the upper part of the water column were examined. Specifically, we undertook detailed examinations using spectral approaches for certain physical quantities.

4.1. Spectral analyses

As explained in the following section, the rotary frequency spectrum (the so-called moored spectrum) was applied to measured currents at several depths (32 m, 98 m, and 210 m), with specific examination of its periodicity and seasonality (Fig. 5). For analysis conducted at 210 m depth, we used data from the single-point current meter S4 (Fig. 5c); for the other two depths (32 m and 98 m), upward-looking ADCP installed at depth of 110 m was used. For the moored spectrum calculation, the FFT method was applied to segments of one month, with 60 degrees of freedom. In the figure, the universal spectrum of internal waves (Garrett and Munk, 1975; designated as GM) is overlaid, giving a reference level of kinetic energy for mid-latitude oceans in terms of the wave frequency.

Overall, a notable peak occurs near the Coriolis frequency at all depths. It is remarkable that marked semidiurnal peaks can be found only in the CW rotation. The current at 32 m (near the bottom of near-surface pycnocline) shows the largest variation of spectral power for higher frequencies among different seasons (Fig. 5a). At 32 m depth, the currents in summer and autumn (Sep.–Nov.; Jun.–Aug.) show the elevation of horizontal kinetic energy, both CW and CCW, compared with the remaining periods. Particularly at frequencies higher than 2f, the current oscillation is more energetic than the GM standard in the two periods. In contrast, the rotary spectra for depths of 98 m and 210 m

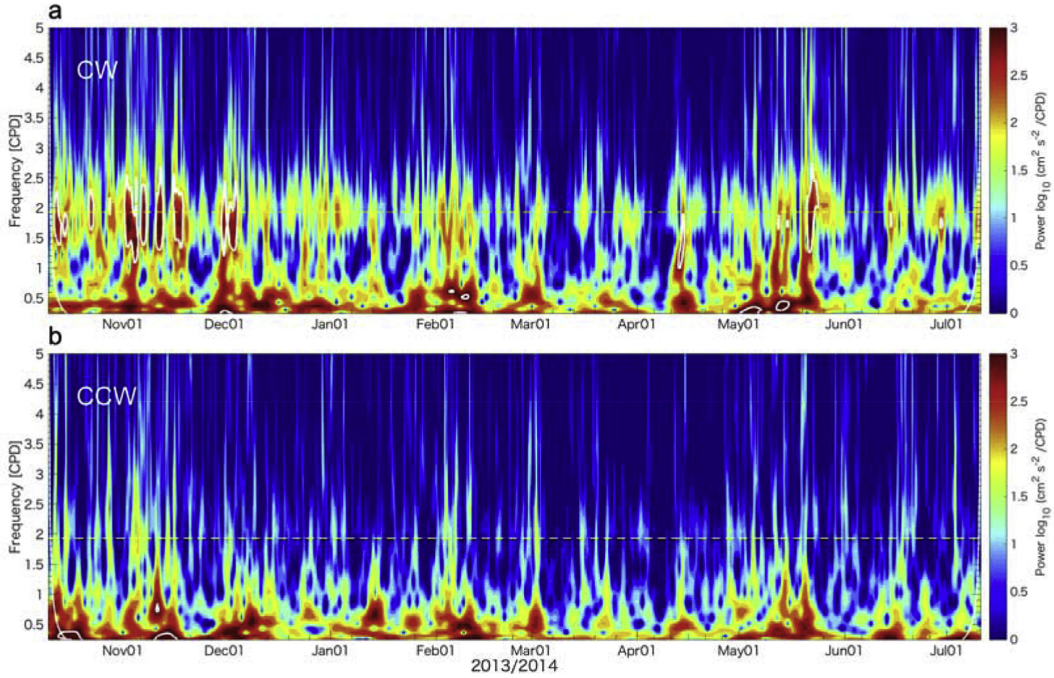

Fig. 4. The Morlet wavelet power spectrum of ice velocity: (a) CW and (b) CCW with time. Values are shown on a logarithmic scale. Bold white curves near the lower corners show the cone of influence. Solid white contour indicates the 95% confidence level. The vertical axis is the frequency in cycles per day (CPD). Yellow, dashed horizontal lines are frequencies of local inertial oscillation of 1.93 CPD. (For interpretation of the references to color in this figure legend, the reader is referred to the Web version of this article.)

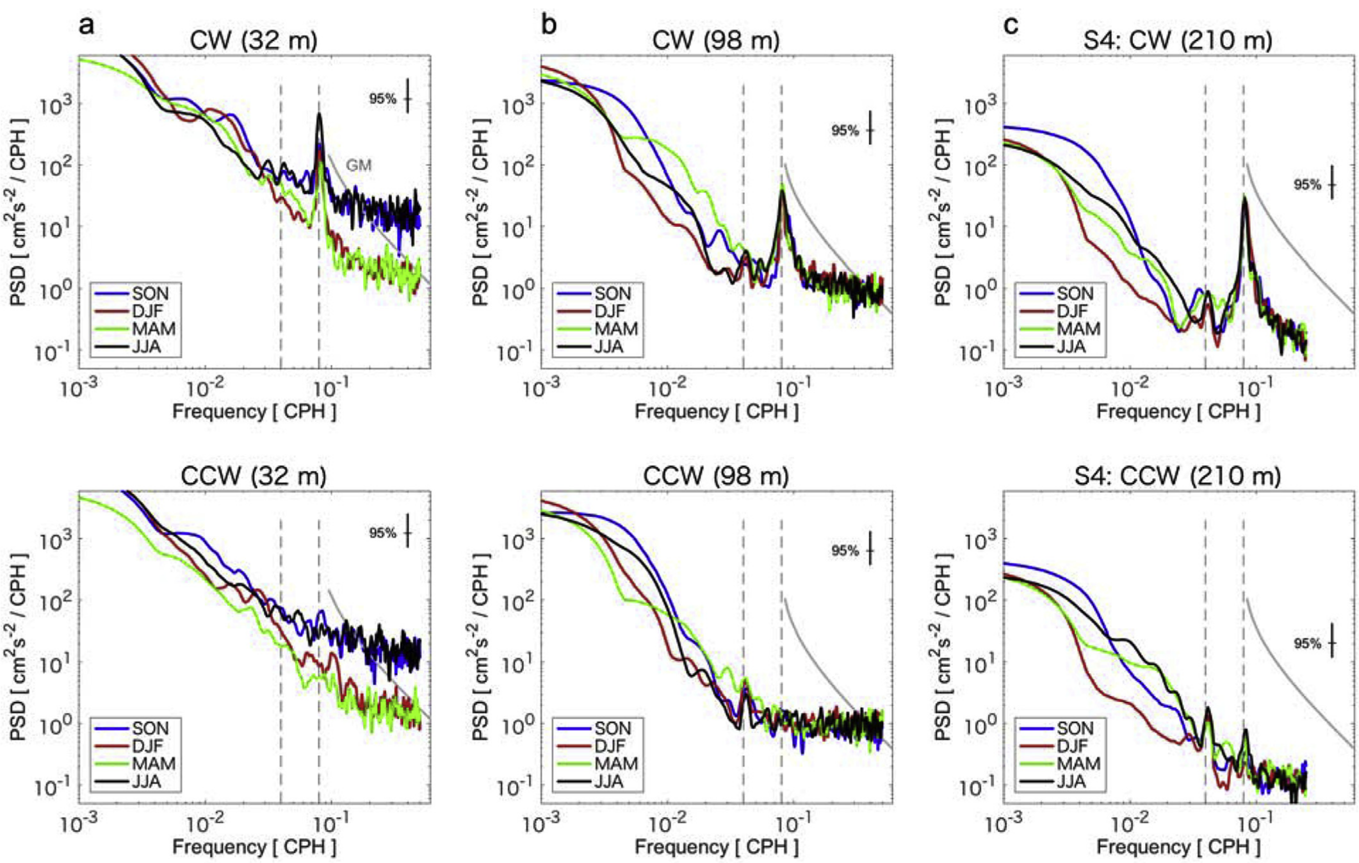

Fig. 5. Rotary spectra of water currents for various periods (SON, DJF, MAM, JJA) at depths of (a) 32 m, (b) 98 m, and (c) 210 m depth. Top and bottom panels respectively portray CW and CCW rotation in terms of time. Results presented in (a) and (b) were obtained from upward-looking ADCP, whereas those in (c) are from the single-point current meter. Vertical dashed lines represent frequencies of *f* and 0.5*f*, respectively corresponding to 12.4 and 24.9 h. The Garrett–Munk (GM) canonical curve is shown as a gray curve. In each panel, a vertical bar denotes the 95% confidence interval, where the degrees of freedom are 60.

show less variability in frequency space among the different seasons.

Furthermore, diurnal oscillation signals were found from the rotary spectrum of the horizontal current, irrespective of depth, season, and rotational direction. The amplitude was even smaller than the near-inertial one which was found for CW (e.g., Fig. 5b and c). According to a barotropic tidal model calculation for the Arctic Ocean (Padman and Erofeeva, 2004), the diurnal oscillation is likely attributable to the O_1 constituent. We also performed the classical tidal harmonic analysis (Pawlowicz et al., 2002) for horizontal currents from the ADCP and S4. According to the analysis, it is confirmed that barotropic tidal current from the O_1 constituent is very sluggish, with the amplitude being even smaller than 1 cm s^{-1} in major axis.

4.2. Wavelet analyses

The previous subsection described examination of the seasonal variation in horizontal current using the rotary spectral analysis. In this subsection, the wave signals at different vertical levels were examined. In this analysis, we detect and analyze heaving motions from vertical displacement of isopycnals surfaces. The density fluctuation, defined by $\Delta\rho(t) = \rho(t) - \bar{\rho}$, is a deviation from a 48-h lowpassed density $\bar{\rho}$. Density is computed from temperature and salinity, as measured using CT sensors (serial numbers: SN2155, SN2156 and SN2163) at nominal depths of 176, 196, and 1320 m. Subtracting the lowpass-filtered density is to mitigate excessive signals associated with mesoscale eddy events. Thereby, the wavelet power may be underestimated at frequencies below 0.5 CPD. The vertical displacement of isopycnals is created using the following formula: $\Delta z(t) = \Delta\rho(t)/\frac{d\rho}{dz}$. The vertical profile of $\frac{d\rho}{dz} = -\frac{\rho}{g}N^2$ was estimated from temperature and salinity profiles of Polar science center Hydrographic Climatology ver. 3 (PHC3.0) (Fig. 7; Steele et al., 2001). PHC3.0 represents the seasonal variation of density and stratification in the upper part of the water column, where it is more (less) stratified in summer (winter) (Fig. 7). Here, the buoyancy frequency N is defined as $N = \left(-\frac{g}{\rho}\frac{\partial\rho}{\partial z}\right)^{1/2}$, and g is the gravitational acceleration.

On the deepest level of 1320 m, the PHC shows very small N, being $\ll$ 1 CPH. Then, division by a near-zero numerator may result in meaningless results. To avoid this, we evenly assumed a basic stratification, being 0.5 CPH, in addition to the monthly variations derived from the PHC3.0.

In Fig. 8, the calculated vertical displacement is shown along the axis of time, particularly addressing a period with an energetic NIW event in late September 2013. Undulating motions in Δz are apparently present, with maximum amplitudes of 5–10 m for the upper two depths and mostly less than 3 m in the deepest one. In general, the wave motions are in phase among the three levels.

The Morlet wavelet power spectra show that the density field at 176 m and 196 m commonly fluctuated with intermittent peaks near the semidiurnal frequency (Fig. 9a and b). Overall, the wavelet signals were relatively weak in late winter (February–April in 2014), but strong in summer (particularly, September in 2013 and 2014). The wavelet shows a certain gap in 176 m and 196 m in amplitude, in which the 196 m looks a bit greater during summertime. We believe that this gap results from a discrepancy for the display of the lower halocline that yields the secondary peak in N. During summer months (July to September), the peak is found at depths between 100 m and 150 m in PHC (Fig. 7), while it is found somewhat deeper in depths between 150 m and 200 m in the *in situ* profile obtained in September 2013 (Fig. 6).

In contrast, the record from the deepest CT sensor (SN2163 at 1320 m depth) shows that near-inertial oscillations in the density field were present only in early October 2013 (Fig. 9c). A remark that can be made about the deepest isopycnal fluctuation is that the near-inertial

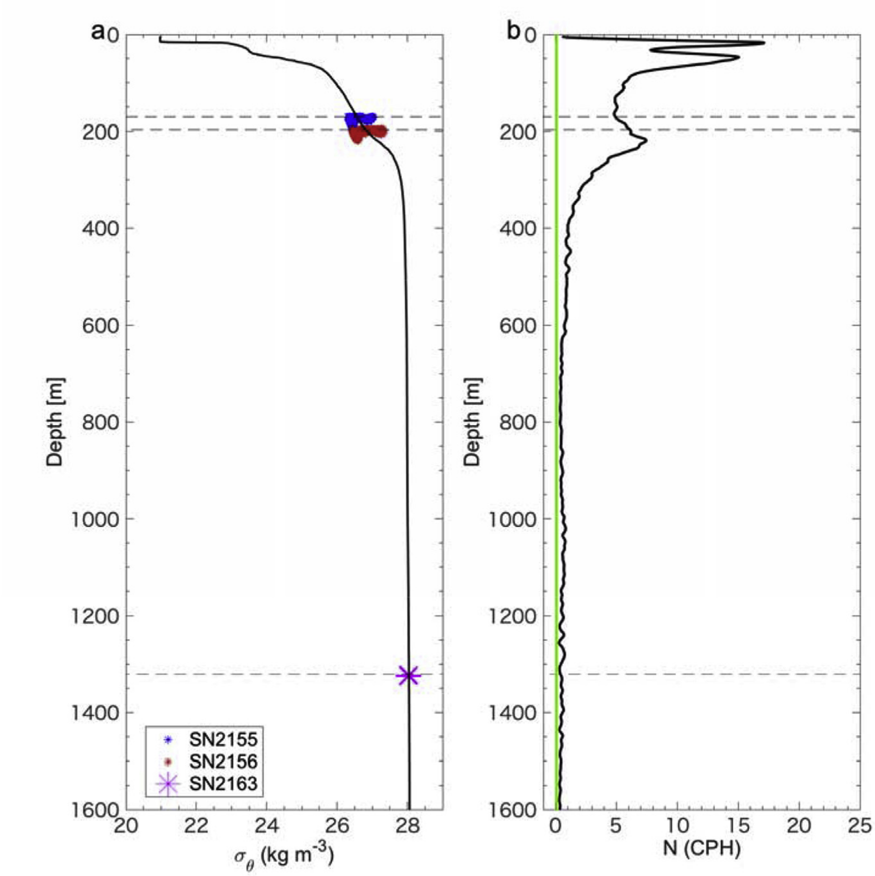

Fig. 6. Vertical profiles of (a) potential density anomaly σ_θ (kg m^{-3}) and (b) buoyancy frequency *N(z)* (cycle per hour, CPH). A vertical profile (black curve) was obtained on September 9, 2013 during the RV Mirai cruise. Hourly records of density from CT sensors are shown as colored symbols, where blue, red, magenta respectively denote records of data at nominal depths of 176, 196, and 1320 m (respectively corresponding to S/N2155, 2156, and 2163). Horizontal dashed lines show average depths of the CT sensors. A vertical green line in (b) shows local *f* of 0.0805 CPH; where N is greater than *f*, the internal waves can propagate. (For interpretation of the references to color in this figure legend, the reader is referred to the Web version of this article.)

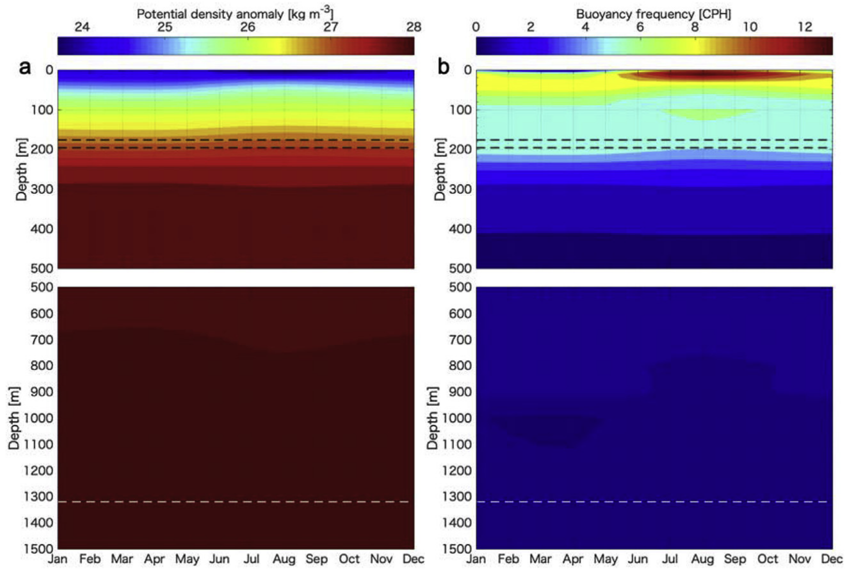

Fig. 7. Monthly climatology of (a) potential density anomaly (kg m^{-3}) and (b) buoyancy frequency (CPH) from PHC 3.0. Data were retrieved at a grid point of (161.5°W, 74.5°N). Horizontal dashed lines show the depths of CT sensors.

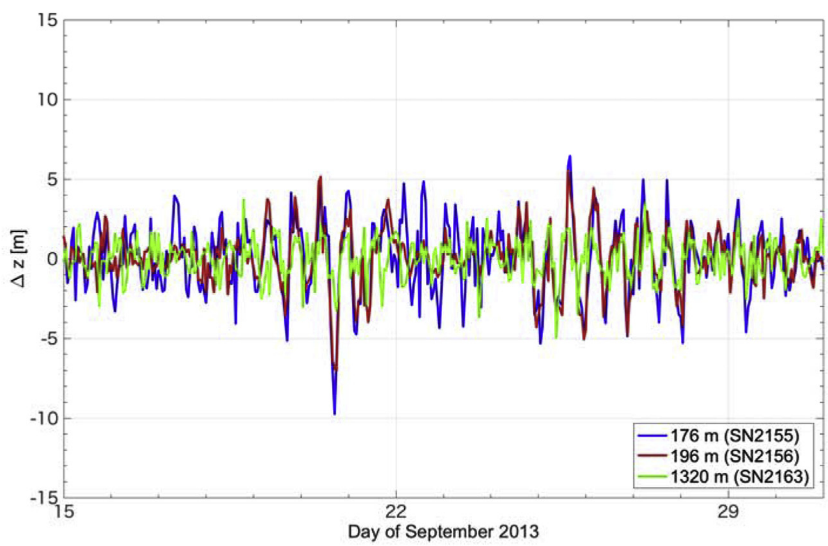

Fig. 8. Lowpass-filtered vertical displacement of CT sensor-installed surfaces respectively at nominal depths of 176, 196, and 1320 m. Results for September 15–30, 2013 are displayed.

peaks appeared about 2–3 weeks after those in the upper layers (Fig. 9a and b). Provided that the near-inertial energy emanates from the surface, the wave's vertical group velocity can be estimated as 50–80 m per day, on average. In Fig. 6b, local stratification seamlessly facilitates internal gravity wave propagation throughout the water column (i.e., f $<$ N; see the green line in Fig. 6b).

From the linear dispersion of near-inertial waves, the vertical group velocity C_{gz} can be derived as $C_{gz} = -k_h^2 \frac{N^2}{\omega k^3}$ (Qi et al., 1995), where k_h is the horizontal wavenumber, k is the vertical wavenumber, and ω is the wave frequency. The absolute value of C_{gz} is evaluated as 77 m per day, giving about 1545 m for 20 days, assuming N = 1.8 CPH (an average over full depth of the profile in Fig. 6b), and 200 m and 10 km, respectively, for the vertical and horizontal wavelengths. The simple estimate for group velocity supports the hypothesis of NIWs originating near the surface and travelling downward through the deep water to 1000 m or greater depth. The choice of 200 m for vertical wavelength may be relevant in the current case (see Section 4.3). The horizontal wavelength of 10 km is based on *in situ* observations from a recent expedition conducted in the Beaufort Sea (Kang, 2014).

4.3. Horizontal current and vertical shear of NIWs

From the spectral analysis described above, it was deduced that the near-inertial waves contributed to the vertical transfer of current energy in the interior water. In this subsection, the temporal variation of horizontal kinetic energy and shear variance, associated with the NIW, will be illustrated.

In this examination, the z axis is replaced by the Wentzel–Kramers–Brillouin (WKB) vertical coordinate of z^* (stretched meters, or sm in the unit): $z^* = \int \frac{N(z)}{N_0} dz$ (Leaman and Sanford, 1975), where the canonical buoyancy frequency, N_0, is 3 CPH. The WKB vertical coordinate is constructed for each month, based on the climatological temperature and salinity of PHC3.0 (Fig. 9). In principle, the WKB scaling procedure minimizes the stretching/shrinking effect of the internal waves because of the variation in density stratification (Leaman and Sanford, 1975). In the WKB coordinate, the 104 m water

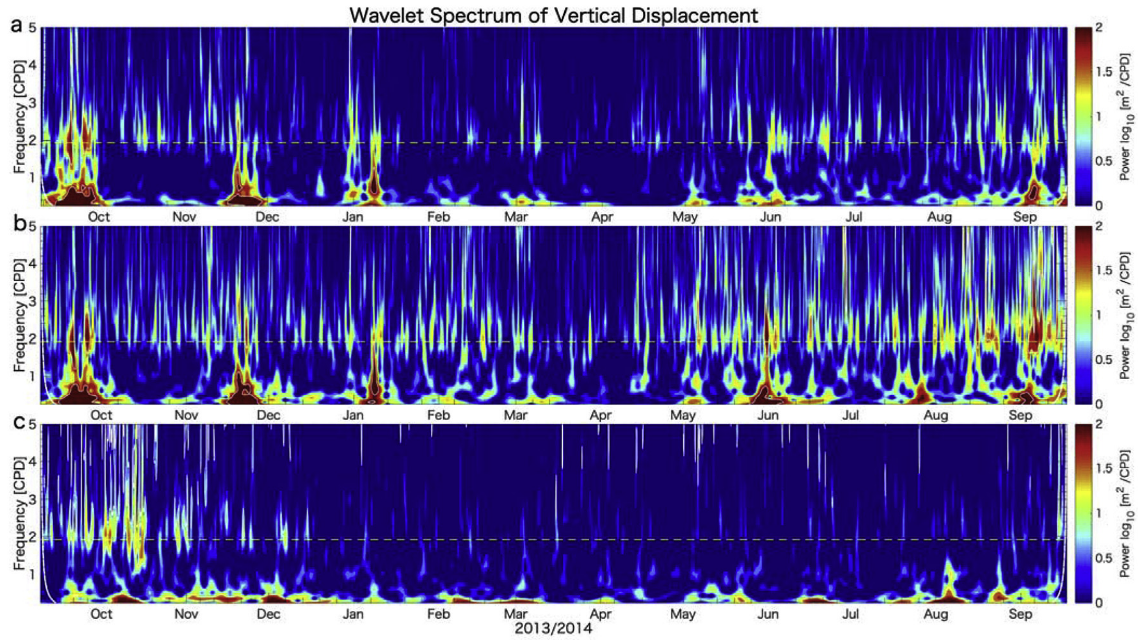

Fig. 9. Morlet wavelet power spectra of vertical displacement, Δz (t), of CT sensors (S/N: 2155, 2156, and 2163), installed respectively at nominal depths of (a) 176 m, (b) 196 m, and (c) 1320 m. Spectral power is shown on a logarithmic scale. Solid white contours show 95% significance levels. Bold white curves at the side bottom show the cone-of-influence level. Yellow, dashed horizontal lines represent the frequencies of local inertial oscillation, i.e. 1.93 CPD. (For interpretation of the references to color in this figure legend, the reader is referred to the Web version of this article.)

column in the real coordinate is mapped onto about 220 stretched meters. Aside from the vertical axis modulation, each component of horizontal current is scaled by the square root of $N(z)/N_0$. In the analysis, the horizontal current is bandpass-filtered over a frequency band of 0.8f–1.2f, and is split into CW and CCW constituents in terms of depth (Leaman and Sanford, 1975; Pinkel, 1984, 2008).

According to Fig. 10b, the near-inertial horizontal current tends to be strong between mid-September and early November 2013, and during May–June, 2014. It is also strongly amplified in September 2014. When it comes to the vertical distribution, the peaks are widely distributed in the former two periods, but are locally concentrated to upper depths in the event of September 2014.

In Fig. 10a, the shear variance is shown separately for upward-travelling and downward-travelling components. The CW and CCW rotation with depth are respectively indicative of downward and upward wave energy propagation (Leaman and Sanford, 1975). The shear spectrum was first created by weighting the vertical wavenumber spectra of the WKB-stretched horizontal current by the factor of $(2\pi k)^2$ (Pinkel, 2008). Then, the shear variance is computed by integrating the power spectrum of the shear over the wavenumbers between 0.0045 and 0.010 CPM (equivalent to 220 m and 40 m, respectively).

In the figure, periods during which the downward-propagating waves are dominant are marked by vertical gray bars. Particularly, the noticeable events with strong shear greater than half the GM are marked by red bars. Throughout the year, downward propagation of NIW is more pronounced than upward propagation, particularly for the periods of September–November 2013 and August–September 2014.

Fig. 11a and b shows the near-inertially bandpassed current in the time-depth coordinate, exhibiting the NIW's wavefront structure in the week-long time frame of November 4–10, 2013. Overall, the downward-travelling group velocity, and consequently the upward-travelling phase velocity, looks more dominant relative to the counterpart of upward-travelling group velocity. A slanting wavefront structure that leads to low phase speed appears around November 4–5.

In Fig. 11c, the two-dimensional spectral density (k versus ω) of the shear is displayed for depths of 20–200 sm (the entire vertical record) during the same time period as that in Fig. 11a and b. Here, two-dimensional Fourier transformation (2DFT) is performed as described by Alford et al. (2012) and Pinkel (1984, 2008). The complex horizontal current (Fig. 11a and b) is converted to shear by weighting by $(2\pi k)^2$ in the spectral space (as shown in Fig. 10a). In the two-dimensional spectral space, the data points in quadrants 1 and 3 denote wave signals with downward-propagating group velocity, whereas those in quadrants 2 and 4 denote signals with upward group velocity. With regard to the frequency field, the CW rotation resides in quadrants 2 and 3, and CCW in quadrants 1 and 4.

The 2DFT analysis confirmed the features shown above: the near-inertial oscillation in the shear, and temporal rotation in the CW sense (the dominant peak exists near $-f$ in quadrants 2 and 3). In the spectral space of vertical wavenumber and frequency, the peak extends vertically in the third quadrant, exhibiting variation in vertical wavenumbers, as suggested in Fig. 11a. The spectral power is particularly elevated for the WKB wavenumbers of $|k| < 0.03$ cpm, being equivalent to $>$ 30 m in absolute wavelength.

5. Discussion

This section addresses the kinetic energy balance in the upper part of the water column. Regarding ADCP horizontal current below 20 m depth, most of the fine-scale kinetic energy is likely attributable to the NIWs emanating from the surface mixed layer. Consequently, the turbulent energy might be produced by internal waves propagating through the interaction of the turbulent Reynolds stress and vertical shear of the mean horizontal velocity.

5.1. Kinetic energy input from ice drift

According to Fig. 3, the ice drift tends to be faster than the water current, which can transfer momentum to the water. To quantify the kinetic energy input into surface water, mixed-layer slab model experiments have been carried out (Pollard and Millard, 1970) (Fig. 12). This model elucidates the evolution of the inertial kinetic energy budget in the surface mixed layer based on the imposed surface momentum flux, i.e. the ice-water stress:

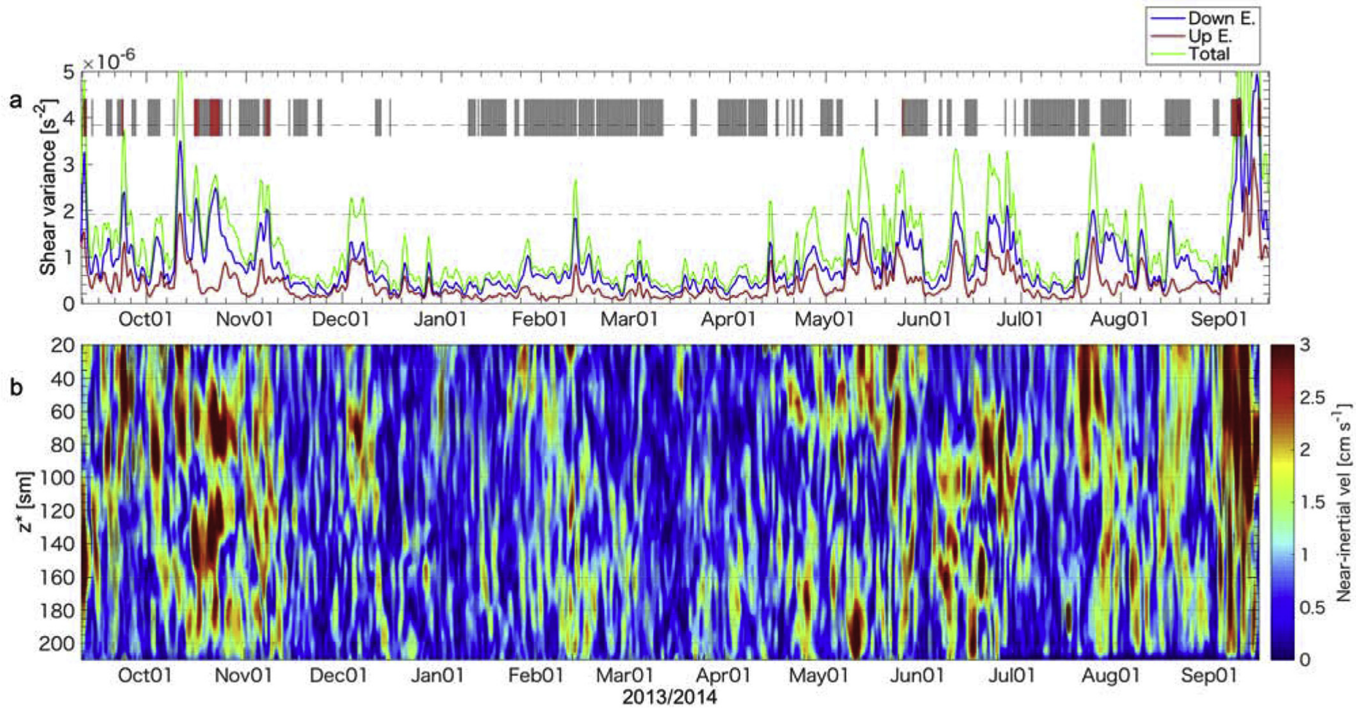

Fig. 10. (a) Time series of vertical shear variance (s^{-2}), where the downward-travelling near-inertial component is shown in blue, upward in red, and total in green; (b) magnitude of near-inertial bandpass-filtered current ($cm\ s^{-1}$). In (a), the shear variance is computed by integrating the spectral energy of horizontal current over a depth range of 20–106 m, after weighting by $(2\pi k)^2$ (see the text). The GM and half GM levels are shown as dashed horizontal lines; vertical grey bars show periods of significant downward-travelling NIW (where the downward kinetic energy is greater than the upward one by a factor of two); red bars represent periods during which the total energy is greater than half of the GM level. In (b), the vertical axis is represented by the WKB coordinate, z^*, in the unit of stretched meters (sm), whereas the current amplitude is scaled by the climatological buoyancy frequency (Fig. 7b). (For interpretation of the references to color in this figure legend, the reader is referred to the Web version of this article.)

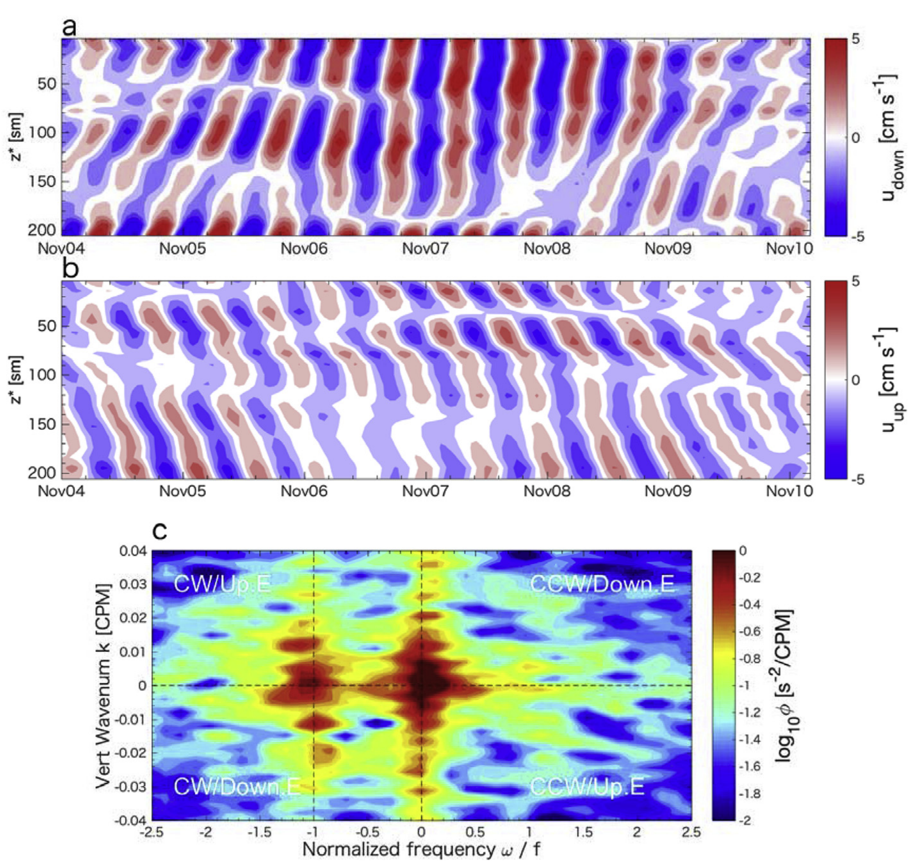

Fig. 11. Near-inertial bandpass horizontal velocity ($cm\ s^{-1}$) for (a) downward and (b) upward energy propagation. In (c), the vertical wavenumber-frequency (k-ω) power spectrum is shown. In (c), data points in quadrants 1 and 3 (2 and 4) show wave packets going downward (upward), whereas quadrants 1 and 4 (2 and 3) respectively show CCW (CW) rotations in time. All panels show data for November 4–10, 2013. In (a) and (b), the wave's vertical phase and amplitude are WKB-scaled based on the climatological buoyancy frequency (Fig. 7b).

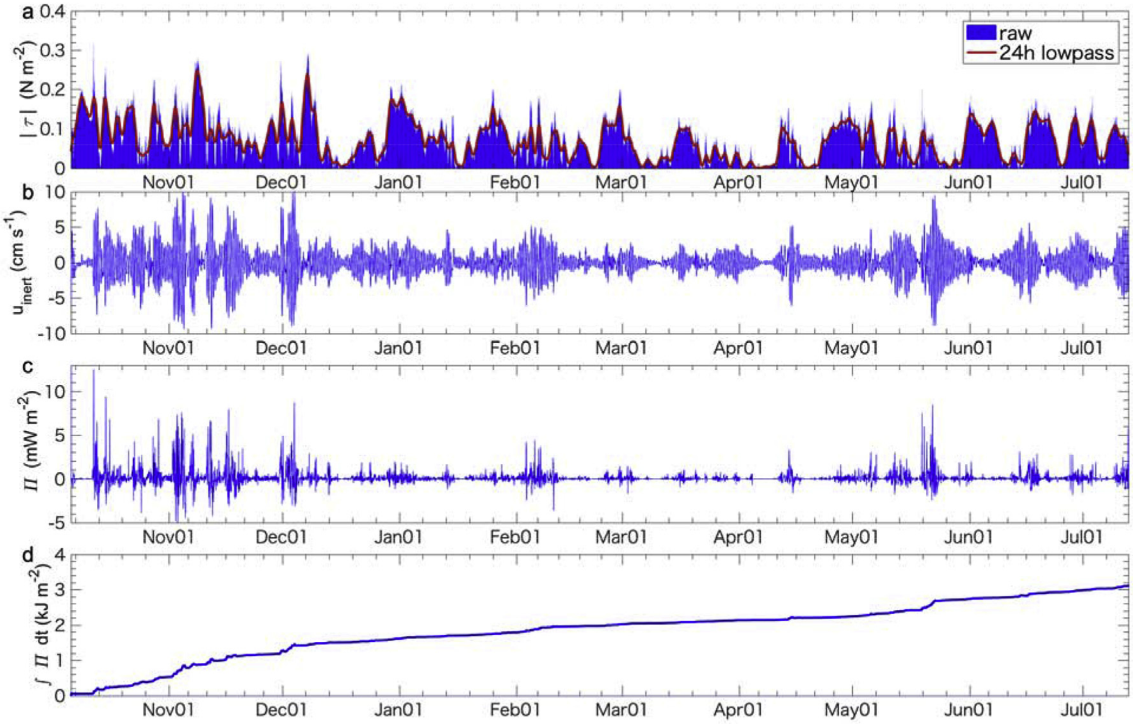

Fig. 12. Results of a mixed-layer slab model experiment: (a) magnitude of ice-to-water stress $|\boldsymbol{\tau}|$ (N m^{-2}), (b) eastward component of mixed-layer inertial velocity u_{inert} (cm s^{-1}), (c) inertial kinetic energy flux Π (mW m^{-2}), and (d) cumulative energy transfer $\int \Pi dt$ (kJ m^{-2}). In (a), a red curve shows 24 h lowpass-filtered data. (For interpretation of the references to color in this figure legend, the reader is referred to the Web version of this article.)

$$\frac{d}{dt}\left(\frac{\rho H_{ML}}{2}|\boldsymbol{Z_I}|^2\right) = -r\rho H_{ML}|\boldsymbol{Z_I}|^2 - \Pi,$$

$$\Pi = Re\left[\rho\frac{\boldsymbol{Z_I}}{\omega^*}\frac{d\tau^*}{dt}\right],$$

where the mixed-layer current velocity $\boldsymbol{Z_I} = \boldsymbol{Z} - \boldsymbol{Z_E}$, the inertial current $\boldsymbol{Z} = u_{inert} + iv_{inert}$ in complex form, the wind-driven Ekman current $\boldsymbol{Z_E} = \tau/\omega H_{ML}$, the ice–ocean interfacial stress $\tau = (\tau_x + i\tau_y)/\rho$, and the oscillation frequency $\omega = r + if$. Here, r is a damping parameter; H_{ML} is the mixed-layer depth. Also Π represents the inertial kinetic energy transfer, being derived as a cross product of the inertial current vector and temporal change of conjugated ice-water stress $\boldsymbol{\tau}^*$. In the model, strong ice drift in phase with the surface current can facilitate inertial oscillation of the mixed layer through the resonance ($\Pi > 0$), whereas the out-of-phase ice drift results in slowing of the inertial oscillation ($\Pi < 0$).

With respect to the ice–ocean interfacial stress, we use the drag law of $\boldsymbol{\tau} = C\rho|\boldsymbol{U_i} - \boldsymbol{U_w}|(\boldsymbol{U_i} - \boldsymbol{U_w})$, where the ice-water drag coefficient C is 5.4×10^{-3} (Shirasawa and Ingram, 1997; Leppäranta, 2005). Also, $\boldsymbol{U_i}$ and $\boldsymbol{U_w}$ respectively denote the velocity of sea ice drift and the mixed-layer water current. The ice velocity $\boldsymbol{U_i}$ is derived from the acoustically measured ice drift (Fig. 2c), whereas $\boldsymbol{U_w}$ is predicted in the model as $\boldsymbol{Z_I}$. When the difference between mixed-layer current and ice velocity, $|\boldsymbol{U_i} - \boldsymbol{U_w}|$, exceeds a threshold of 10 cm s^{-1} in magnitude, it is *a priori* set to be 10 cm s^{-1}. The model implements the computation at a time step interval of 1 h. This 1-h resolution of measured surface stress is adequate for the slab model experiment (c.f., 3 h in D'Asaro, 1985). For calculations, H_{ML} is assumed to be constant at 20 m. The constant r is an inverse of characteristic damping time scale. The model computation is conducted for the completely ice-covered period: October 2013 through July 2014. The choice of mixed-layer depth and damping parameter can engender approximate error of 10–20% in the results of energy flux. The default combination of $H_{ML} = 20$ m and $r = 1/3.5$ day gives accumulated kinetic energy of 3.1 kJ m^{-2} over the year. The evaluation can be shifted to 3.8 kJ m^{-2} and 2.8 kJ m^{-2} with H_{ML} of 15 m and 50 m, respectively. Cases with $r = 1/3.0$ day and $1/4.0$ day respectively give 3.2 kJ m^{-2} and 3.0 kJ m^{-2}.

The experiment demonstrates that the magnitude of mixed-layer inertial oscillation directly responds to the strength of ice-water stress (Fig. 12a and b). In the autumn of the first year, the mixed-layer inertial current is particularly strong in association with the swift sea ice drift. That phenomenon is associated with weak internal stress because of the low ice concentration (Fig. 2a). The most prominent events of ice-to-water energy input recurrently take place during October to early December (Fig. 12c). The wavelet of ice drift during this period showed considerably high levels of inertial motion in ice drift (Fig. 4). The slab model simulates that even during mid-winter (early February), the inertially oscillating sea-ice drift produced a certain amount of kinetic energy input, being 1–3 mW m^{-2}, into ocean surface, resulting in the generation of inertial oscillation at the underice SML. With respect to the buildup of surface kinetic energy flux, one can explain it by the resonance between the inertial ice drift and the near-inertial surface water current. Regarding the integral amount of Π, nearly 60% of the annual inertial energy budget was earned over the first two months, i.e., during mid-October to early December 2013 (Fig. 12d).

5.2. Turbulent kinetic energy dissipation in the upper part of the water column

Next, we discuss dissipation of turbulence energy resulting from the fine-scale kinetic energy of NIW in the upper part of the water column. The semi-empirical fine-scale parameterization of NIW (Henyey et al., 1986; Gregg, 1989) can be useful to estimate the approximate magnitude of kinetic energy dissipation rate, ε, as

$$\varepsilon = 7 \times 10^{-10}\left(N^2/N_0^2\right)\left(S_{10}^4/S_{GM}^4\right)j(f/N),$$

where $S_{GM} = 3.6 \times 10^{-3}\left(N^2/N_0{}^2\right)^{1/2}$. The scaling factor $j(N/f)$ is defined by $j\left(\frac{f}{N}\right) = \cosh^{-1}(N/f)/f_{30}\ \cosh^{-1}(N_0/f_{30})$, parameterizing the latitudinal

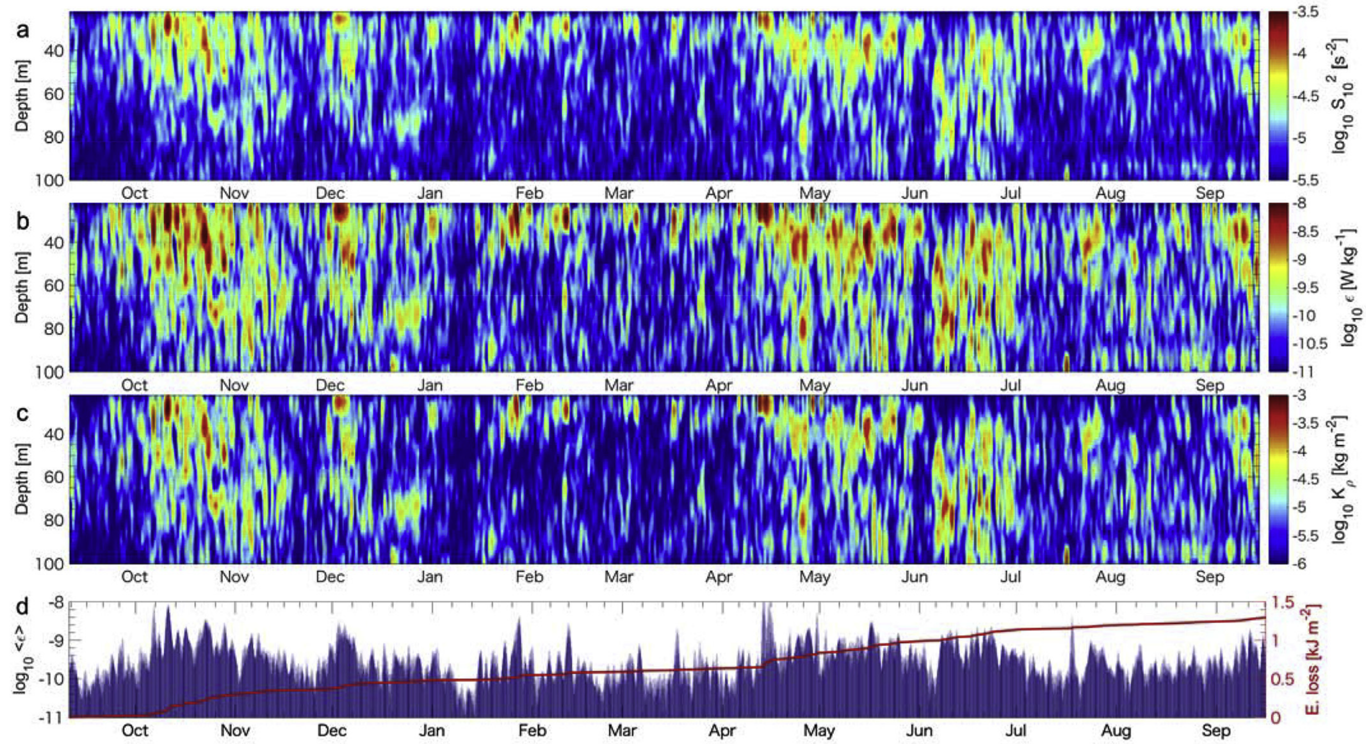

Fig. 13. Time-vertical sections of (a) the square of 10-m scale vertical shear S_{10} (s^{-2}), (b) estimated ε (W kg^{-1}), (c) vertical turbulent diffusivity K_ρ (kg m^{-2}), and (d) depth-averaged ε (blue vertical bars) and its integral over time (kJ m^{-2}) in red. Fine-scale parameterization (Gregg, 1989) is applied to the near-inertial horizontal current (0.8–1.2*f*), where the vertical profile of *N(z)* is inferred from monthly climatology (Fig. 7b). (For interpretation of the references to color in this figure legend, the reader is referred to the Web version of this article.)

dependency of turbulence relative to the empirical values at 30°N. Based on PHC3.0, the term of $j(N/f)$ is proportional to *N*, varying between 1.9 and 2.2. According to Gregg (1989), the estimate for turbulence is accurate to within a factor of about 2. For calculations, we used the 10-m lowpass-filtered vertical shear of ADCP horizontal current (S_{10}) and vertical profiles of time-varying buoyancy frequency, *N(z)*, based on the PHC climatology (Fig. 7b). Turbulent diffusivity was estimated as $K_\rho = \Gamma\frac{\varepsilon}{N^2}$, where Γ is the efficiency factor, assumed to be 0.2 (Ellison, 1957). In what follows, ε and K_ρ are estimated based on the near-inertially bandpassed horizontal current (0.8f–1.2f) (Fig. 10b). Note that WKB scaling is not applied to this calculation.

The calculation results of vertical shear, ε, and K_ρ are presented in Fig. 13. In Fig. 13d, ε is also illustrated by its vertical average (blue bars). In general, the spatiotemporal patterns of ε and K_ρ resemble that for the vertical shear in Fig. 13a: the turbulent variables are high in summer and autumn, and low in the mid-winter. The turbulent energy maxima were mostly seen in the upper 50 m, having an order of magnitude of $10^{-8.5}$ W kg^{-1} for ε and 10^{-4} $m^2\,s^{-1}$ for K_ρ (Fig. 13b; c).

It is surprising that the turbulence energy is low in September 2014, being $\varepsilon = O(10^{-10}$ W $kg^{-1})$ and $K_\rho = O(10^{-5}$ $m^2\,s^{-1})$ (Fig. 13b and c), contrary to the NIW's horizontal kinetic energy attaining the greatest level (e.g. Fig. 10b). The relatively weak turbulence is likely attributable to the modest signal of vertical shear in the fine-scale wave structure (Fig. 13a).

The temporal accumulation of vertically averaged ε reveals that the kinetic energy losses are markedly earned by 0.5 kJ m^{-2} until the end of November, followed by the least losses during winter season (Fig. 13d). Then, it pronouncedly increased again in April–June 2014. The total energy loss of 1.3 kJ m^{-2} is roughly 42% of the total amount of inertial kinetic energy input when the sea ice exists, being 3.1 kJ m^{-2} (Fig. 12d). It is anticipated that some part of the remaining incoming energy is consumed for evolution of the surface mixed layer, i.e., kinetic-to-potential energy conversion through destruction of stratified layers near its base. To evaluate the validity of the estimates above, direct microstructure measurements must be carried out in a similar environment.

6. Concluding remarks

We conducted year-round observations of sea-ice variables (concentration, draft, and drift) and water current in the upper part of the water column. Two acoustic devices (IPS and ADCP) were moored in the Northwind Abyssal Plain, Arctic Ocean. The IPS-ADCP coupling system documented the seasonal evolution of ice draft, the initial freezing of open water in the autumn (particularly October), followed by nearly linear ice growth in mid-winter (November–May), and finally the most rapid decay in mid-summer (July–August) in the following year (Fig. 2). Mean ice drift is typically northeastward, roughly following the local bathymetry (Fig. 3). The rapid ice drift is characterized by semi-diurnal inertial motion (Fig. 4). The wavelet spectrum documents that the energetic peak near the inertial frequency comes in the late autumn of the ice-forming season, and in early summer, during the melting season.

The ADCP measurements showed that the water current in the vertical range of 20–104 m depth responds to the semi-diurnal ice motion. Near-inertial waves were most pronouncedly generated in the fall and early summer, when sea ice was thin and its drift was swift in terms of inertial oscillation. During this period, the NIW's kinetic energy tends to be transferred downward (Fig. 10). In water deeper than 1000 m, temperature and salinity records indicate that near-inertial fluctuations are only detectable during the period in the absence of sea ice (Fig. 9c).

According to the fine-scale parameterization of turbulent kinetic energy dissipation (Gregg, 1989), NIWs caused elevation in the dissipation rate and the eddy diffusivity in the upper part of the water column (Fig. 13). These variables are estimated as ε = O

($10^{-8.5}$ W kg^{-1}) and $K_\rho = O(10^{-4}$ kg m^{-2}). Finally, a back-of-the-envelope calculation of near-inertial energy flow, over the vertical range from sea ice and the upper part of the water column, suggests that around 42% of the surface energy input resulting from the ice–water velocity difference is lost as the waves travel through the upper part of the water column. In future studies, estimates of turbulent parameters should be evaluated though comparison with direct microstructure measurements.

Acknowledgments

The mooring NAP13t deployment was conducted by RV Mirai of Japan Agency for Marine-Earth Science and Technology. The recovery was done by CCGS Amundsen in the framework of the ArcticNet 2014. We thank the captain and crew of the ships for their professional engagement. The RV Mirai Arctic cruise was performed under support from the Green Network of Excellence (GRENE) Program/Arctic Climate Change Research Project and the Arctic Challenge for Sustainability (ArCS) Project of the Ministry of Education, Culture, Sports, Science and Technology of Japan. Preparation of the IPS-ADCP system and the data post-processing were performed under the Joint Research Program of the Institute of Low Temperature Science, Hokkaido University, and the Joint Research Program of the Japan Arctic Research Network Center. This study is partly supported by a Grant-in-Aid for Scientific Research of the Japan Society for the Promotion of Science KAKENHI Grants no. 16H01596 (JPY2016-2018) and 16K21700 (JPY2016-2019) to Y. Kawaguchi, 15H05712 (JPY2015-2019) to N. Harada. The authors are grateful to two anonymous reviewers for their fruitful discussions and meticulous reading. Their comments greatly improved the accuracy of the internal wave analyses.

References

Alford, M.H., Cronin, M.F., Klymak, J.M., 2012. Annual cycle and depth penetration of wind-generated near-inertial internal waves at ocean station Papa in the Northeast Pacific. J. Phys. Oceanogr. 42, 889–909. https://doi.org/10.1175/JPO-D-11-092.1.

Belliveau, D.J., Bugden, G.L., Eid, B.M., Calnan, C.J., 1990. Sea ice velocity measurements by upward-looking Doppler current profilers. J. Atmos. Ocean. Technol. 7, 596–602.

Birch, R., Fissel, D., Melling, H., Vaudrey, K., Schaudt, K., Heideman, J., Lamb, W., 2000. Ice-profiling sonar. Sea Technol. 41 (8), 5.

D'Asasro, E.A., Morison, J.H., 1992. Internal waves and mixing in the Arctic Ocean. Deep-Sea Res. 39A, S459–S484. https://doi.org/10.1016/S0198-0149(06)80016-6.

D'Asaro, E.A., 1985. The energy flux from the wind to near-inertial motions in the surface mixed layer. J. Phys. Oceanogr. 43, 1043–1059.

D'Asaro, E.A., Morehead, M.D., 1991. Internal waves and velocity fine structure in the Arctic Ocean. J. Geophys. Res. 96, 12725–12738. https://doi.org/10.1029/91JC01071.

Ellison, T.H., 1957. Turbulent transport of heat and momentum from an infinite rough plane. J. Fluid Mech. 2, 456–466.

Fukamachi, Y., 2009. Direct observations of sea-ice thickness and brine rejection off Sakhalin in the Sea of Okhotsk. Cont. Shelf Res. 29, 1541–1548. https://doi.org/10.1016/j.csr.2009.04.005. 9 coauthors.

Fukamachi, Y., Mizuta, G., Oshima, K.I., Melling, H., Fissel, D., Wakatsuchi, M., 2003. Variability of sea-ice draft off Hokkaido in the Sea of Okhotsk revealed by a moored ice-profiling sonar in winter of 1999. Geophys. Res. Lett. 30 (7), 1376. https://doi.org/10.1029/2002GL016197.

Garrett, C.J.R., Munk, W.H., 1975. Space-time scales of internal waves: a progress report. J. Geophys. Res. 80, 291–297. https://doi.org/10.1029/JC080i003p00291.

Gregg, M., 1989. Scaling turbulent dissipation in the thermocline. J. Geophys. Res. 94, 9686–9698.

Henyey, F.S., Wright, J., Flatté, S.M., 1986. Energy and action flow through the internal wave field: an eikonal approach. J. Geophys. Res. 91, 8487–8495.

Inoue, J., Hori, M.E., 2011. Arctic cyclogenesis at the marginal ice zone: A contributory mechanism for the temperature amplification? Geophys. Res. Lett. 38https://doi.org/10.1029/2011GL047696. L12502.

Kang, S.H., 2014. Cruise Report – IBRV Araon ARA05B 2014. KOPRI.

Kawaguchi, Y., Hutchings, J.K., Kikuchi, T., Morison, J.H., Krishfield, R.A., 2012. Anomalous sea-ice reduction in the Eurasian basin of the Arctic Ocean during summer 2010. Polar Sci. 6, 39–53. https://doi.org/10.1016/j.polar.2011.11.003.

Kawaguchi, Y., Nishino, S., Inoue, J., Maeno, K., Takeda, H., Oshima, K., 2016. Enhanced diapycnal mixing due to near-inertial internal waves propagating through an anticyclonic eddy in the ice-free Chukchi Plateau. J. Phys. Oceanogr. 46 (8), 2457–2481. https://doi.org/10.1175/JPO-D-15-015.1.

Krishfield, R.A., Tool, J., Proshutinsky, A., Timmermans, M.-L., 2008. Automated ice-tethered profilers for seawater observations under pack ice in all seasons. J. Atmos. Ocean. Technol. 25, 2091–2095. https://doi.org/10.1175/2008JTECHO587.1.

Krishfield, R.A., Proshutinsky, A., Tateyama, K., Williams, W.J., Carmack, E.C., McLaughklin, F.A., Timmermans, M.-L., 2014. Deterioration of perennial sea ice in the Beaufort Gyre from 2003 to 2012 and its impact on the oceanic freshwater cycle. J. Geophys. Res. Oceans. 119, 1271–1305. https://doi.org/10.1002/2013 JC008999.

Leaman, K.D., Sanford, T.B., 1975. Vertical energy propagation of internal waves: a vector spectral analysis of velocity profiles. J. Geophys. Res. 80, 1975–1978. https://doi.org/10.1029/97JC03200.

Leppäranta, M., 2005. The Drift of Sea Ice. Springer, pp. 266.

Martini, K.I., Simmons, H.L., Stoudt, C.A., Hutchings, J.K., 2014. Near-inertial internal waves and sea ice in the Beaufort Sea. J. Phys. Oceanogr. 44, 22122234. https://doi.org/10.1175/JPO-D-13-0160.1.

McPhee, M., 2008. Air–ice–ocean Interaction "Turbulent Ocean Boundary Layer Exchange Processes". Springer, pp. 215.

Padman, L., Erofeeva, S., 2004. A barotropic inverse tidal model for the Arctic Ocean. Geophys. Res. Lett. 31, L02303. https://doi.org/10.1029/2003GL019003.

Padman, L., Kottmeier, C., 2000. High-frequency ice motion and divergence in the Weddell Sea. J. Geophys. Res. 105 (C2), 3379–3400.

Pawlowicz, R., Beardsley, B., Lentz, S., 2002. Classical tidal harmonic analysis including error estimates in Matlab using t_tide. Comput. Geosci. 28, 929–937.

Pinkel, R., 1984. Doppler sonar observations of internal waves: the wavenumber frequency spectrum. J. Phys. Oceanogr. 14, 1249–1270.

Pinkel, R., 2005. Near-inertial wave propagation in the western Arctic. J. Phys. Oceanogr. 35, 645–665.

Pinkel, R., 2008. The wavenumber–frequency spectrum of vertical and internal wave shear in the western Arctic Ocean. J. Phys. Oceanogr. 38, 277–290. https://doi.org/10.1175/2006JPO3558.1.

Pollard, R.T., Millard, R.C., 1970. Comparison between observed and simulated wind-generated inertial oscillations. Deep-Sea Res. Oceanogr. Abstr. 17, 813–816. https://doi.org/10.1016/0011-7471(70)900430-4.

Qi, H., De Szoeke, R.A., Paulson, C.A., Erikson, C.C., 1995. The structure of near-inertial waves during ocean storms. J. Phys. Oceanogr. 25, 2853–2871.

Rainville, L., Woodgate, R.A., 2009. Observations of internal waves generation in the seasonally ice-free Arctic. Geophys. Res. Lett. 36, L23604. https://doi.org/10.1029/2009GL041291.

Shirasawa, K., Ingram, R.G., 1997. Currents and turbulent fluxes under the first-year sea ice in Resolute Passage, Northwest Territories, Canada. J. Mar. Syst. 11, 21–32.

Steele, M., Morley, R., Ermold, W., 2001. PHC – a global ocean hydrography with a high quality Arctic Ocean. J. Clim. 14, 2079–2087.

Vivier, F., Hutchings, J.K., Kawaguchi, Y., Kikuchi, T., Morison, J.H., Lourenço, A., Noguchi, T., 2016. Sea ice melt onset associated with lead opening during spring/summer transition near the North Pole. J. Geophys. Res. Oceans 121. https://doi.org/10.1002/2015JC011588.

Zippel, S., Thomson, J., 2016. Air-sea interactions in the marginal ice zone. Element. Sci. Anthropocene 4https://doi.org/10.12952/journal.elementa.000095. 000095.